Pan *et al. Biochar* (2024) 6:93
https://doi.org/10.1007/s42773-024-00392-5

Biochar

ORIGINAL RESEARCH Open Access

Preparation of nano Cu-Mo_2C interface supported on ordered mesoporous biochar of ultrahigh surface area for reverse water gas shift reaction

Xueyuan Pan[1], Hao Sun[1*], Mingzhe Ma[1], Haiquan Liao[1], Guowu Zhan[2*], Kui Wang[1,3*], Mengmeng Fan[3], Jingcheng Xu[3], Linfei Ding[3], Kang Sun[1] and Jianchun Jiang[1]

Abstract

High conversion rate and selectivity are challenges for CO_2 utilization through catalytic reverse water gas shift (RWGS) reaction. Herein, a novel mesoporous biochar (MB) supported Cu-Mo_2C nano-interface was prepared by consecutive physical activation of coconut shells followed by carbothermal hydrogen reduction of bimetal. As compared with traditional carbon materials, this MB exhibited ultra-high specific surface area (2693 $m^2\ g^{-1}$) and mesopore volume of mesopore (0.81 $cm^3\ g^{-1}$) with a narrow distribution (2–5 nm), responsible for the high dispersion of binary Cu-Mo_2C sites, CO_2 adsorption and mass transfer in the reaction system. Moderate carbothermal reduction led to the sufficient reduction of Mo ion with carbon matrix of MB and dispersive growth of nano Cu-Mo_2C binary sites (~6.1 nm) on the surface of MB. Cu^+ species were formed from Cu^0 via electron transfer and showed high dispersion with simultaneous boosted bimetal loading due to the strong interaction between nano Mo_2C and Cu. These were advantageous to the intrinsic activity and stability of the Cu-Mo_2C binary sites and their accessibility to the reactant molecules. Under the RWGS reaction conditions of 500 °C, atmospheric pressure, and 300,000 ml/g/h gas hour space velocity, the CO_2 conversion rate over Cu-Mo_2C/MB reached 27.74×10^{-5} $mol_{CO2}/g_{cat}/s$ at very low H_2 partial pressure, which was more than twice that over traditional carbon supported Cu-Mo_2C catalysts. In addition, this catalyst exhibited 99.08% CO selectivity and high stability for more than 50 h without a decrease in activity and selectivity. This study offers a new development strategy and a promising candidate for industrial RWGS.

Highlights

- Coconut shell derived ordered mesoporous biochar with ultra-high S_{BET} and mesopore volume was fabricated.
- Mesoporous biochar facilitates nano Cu-Mo_2C interface formation, CO_2 adsorption and mass transfer.
- Strong interaction between Mo_2C and Cu leads to electron transfer and anchoring of Cu.
- CO_2 conversion rate over Cu-Mo_2C/MB was twice that over Cu-Mo_2C/traditional carbon.
- The catalyst exhibited 99.1% CO selectivity and high stability for more than 50 h.

*Correspondence:
Hao Sun
sunhao@icifp.cn
Guowu Zhan
gwzhan@hqu.edu.cn
Kui Wang
wangkui@caf.ac.cn
Full list of author information is available at the end of the article

Keywords CO_2 utilization, Reversed water gas shift, Cu-Mo_2C interface, Mesoporous biochar, High conversion rate

Graphical Abstract

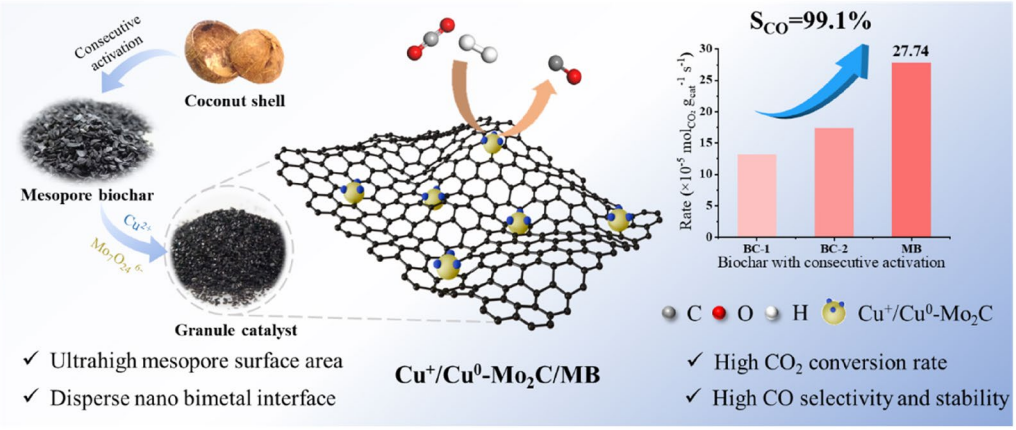

1 Introduction

In the twenty-first century, climate change and ocean acidification due to excessive CO_2 emissions have posed a serious threat to the biological environment and mankind of the entire planet (Tawalbeh et al. 2023). The economical and efficient utilization of CO_2 remains an urgent task for addressing the challenge of climate change (Len et al. 2023; McLaughlin et al. 2023). The CO_2 hydrogenation and emerging electroreduction approaches could convert the CO_2 to other useful products, which turn CO_2 from a terminator of fossil energy usage into value-added chemicals and energy carriers as well as a participant in carbon recycling (Ahmadi Khoshooei et al. 2024; Li et al. 2022). It offers significant economic value and potential for industrial application in addressing the issues of CO_2 emissions and energy scarcity (Song et al. 2023; Wu et al. 2022).

Compared with high-pressure conversion processes such as CO_2 to methanol, the reverse water gas shift (RWGS) reaction is one of the most promising methods for large-scale transformation of CO_2 with high selectivity and low operating pressure. Meanwhile, CO is an intermediate in hydrothermal processes (Fischer–Tropsch synthesis or other syngas technologies) for the production of various high-value added chemicals like methanol, olefins, fuels, and polymers (Liu et al. 2022, 2020; Wang et al. 2023a, 2023b).

At present, the catalysts used in the RWGS reaction mainly include Cu-based catalysts (Kunkes et al. 2015), Ni-based catalysts (Mejia et al. 2018), noble metal-based catalysts, and composite metal catalysts (Posada-Perez et al. 2016). Among them, Cu-Mo_2C-based catalysts exhibit excellent catalytic activity and selectivity (Reddy et al. 2019; Zhang et al. 2021). The existing preparation methods of Mo_2C composite catalysts generally use molybdenum oxide as precursors, and CH_4, CO, or other low-carbon gases as carbon sources to carry out reduction carburizing reactions in the hydrogen atmosphere (Juneau et al. 2020; Liu et al. 2016). However, the coke generated from the pyrolysis of low carbon gas at low temperature will be deposited on the surface of carbides, and the specific surface area of Mo_2C is reduced. Xiong et al. used sodium alginate as a carbon source for carburizing to improve the specific surface area of Cu-Mo_2C based-catalysts. However, its specific surface area and space time conversion of CO_2 hydrogenation to CO still need improvement (Xiong et al. 2018). Moreover, owing to the low mechanical strength of Cu-Mo_2C-based catalysts, additional high-pressure molding for the catalysts is required before the continuous fixed bed reaction.

Compared with hydrocarbon organics, porous biochar prepared from forest processing residues has the dual functions of carbon source and support, and its high thermochemical stability can avoid the formation of polymerized carbon coke that blocks the pore and covers the active center. At the same time, it also has the advantages of large specific surface area and pore volume, adjustable surface groups, pore size distribution and strength, controllable surface metal distribution, and easy recovery (Chen et al. 2021; Gawande et al. 2020). In our past work, commercial mesoporous biochar powder was utilized as a carbon source to prepare mesoporous

biochar-based Mo_2C by carbothermal hydrogen reduction method, which can increase the specific surface area of the catalyst to 337 m^2g^{-1} and promote the dispersion of Mo_2C active sites, thus improving the density of the effective active sites and accessibility of reaction molecules (Wang et al. 2019). However, the simultaneous formation mechanism of Cu and Mo_2C on the surface of mesoporous biochar support and the interaction between them remain to be further studied, as well as the specific surface area and mesopore volume of mesoporous biochar still need to be promoted.

It is well known that hard coconut shell residues are useful for the preparation of granular biochar-based catalysts with controllable pore structure and high performance (Borghei et al. 2017; Sun et al. 2021). Therefore, a coconut shell-derived granule mesoporous biochar (MB) with high mechanical strength, ultrahigh specific surface area, and narrow-mesopore volume was designed by a consecutive physical activation method. Utilizing excellent support and carbon source function for MB, the Cu-Mo_2C/MB catalyst was simultaneously synthesized by a carbothermic hydrogen reduction. The dispersion growth mechanism and interaction of nano Mo_2C and Cu on MB surface were revealed under various carburizing temperatures and bimetal ratios. Moreover, the relationship between the structure and catalytic performance of the RWGS reaction was further investigated.

2 Experimental

2.1 Materials

Copper nitrate trihydrate ($Cu(NO_3)_2{\cdot}3H_2O$), ammonium molybdate tetrahydrate ($(NH_4)_6Mo_7O_{24}{\cdot}4H_2O$), and hydrogen peroxide (H_2O_2) were purchased from Macklin Inc. Coconut shells were collected in Hainan Province. All chemical solutions were prepared using deionized (DI) water.

2.2 Catalyst preparation

Catalyst support preparation: MB granule was prepared by three consecutive physical activation with steam (Sun et al. 2022). The coconut shells were carbonized at 550 °C for 2 h, and then the activation process for coconut shell charcoal was carried out at 900 °C under stream for 1 h. After three consecutive activations, the resulting sample was washed with acid and deionized water until pH = 6–7. Before the introduction of metal sites, MB was pretreated with 30 wt.% of H_2O_2 under stirring at 50 °C for 5 h. The solid was further dried in a vacuum oven at 80 °C for 12 h. For comparison, the biochar with one activation and with two consecutive activations were denoted as BC-1 and BC-2.

Cu-Mo_2C/MB catalysts preparation: Cu-Mo_2C/MB precursor was synthesized using an incipient impregnation method. Typically, the aqueous solutions of $(NH_4)_6Mo_7O_{24}{\cdot}4H_2O$ and Cu $(NO_3)_2{\cdot}3H_2O$ were mixed under stirring at room temperature, and then pretreated MB granule was immersed into the prepared mixture. This mixture was further impregnated at room temperature for 24 h and then dried at 80 °C for 12 h under vacuum. In order to determine the optimal Cu-Mo ratio, the Mo loading was 20 wt.% in all cases, while Cu loading was varied in the range of 0.6 to 1.4 wt.%. The suitable Cu-Mo ratio of 0.8:20 was obtained according to the test of RWGS catalytic performance over Cu-Mo_2C/MB-800 catalysts. Then the metal content was adjusted synchronously to obtain the optimal metal utilization rate. Subsequently, Cu-Mo_2C/MB granule catalysts were prepared by the carbothermal hydrogen reduction method. The resultant samples were placed into a tube furnace under a 10% H_2/N_2 flow at 800 °C for 2 h. Finally, the sample was cooled down to room temperature and passivated with 1% O_2/N_2 for 2 h. In this way, samples were prepared and labeled according to the metal loading amount and carburization temperatures: *y*wt.%Cu-*z*wt.%Mo_2C/MB-X (*y* and *z* represent the amount of loaded metal, X represents the carburizing temperature). The Cu-Mo_2C/MB is used for general representation of catalysts prepared at different carbonization temperatures and bimetal contents.

2.3 Catalyst characterization

The surface area and pore volume were measured on an ASAP 2460 (Micromeritics, America) volumetric adsorption apparatus at 77 K using liquid N_2. Micropore volume (V_{micro}), mesopore volume (V_{meso}), and macropore volume (V_{macro}) were obtained according to the non-local density functional theory (NLDFT). The total surface area (S_{BET}) and pore volume (V_{total}) were obtained according to Brunauer–Emmett–Teller (BET) method and volume absorbed at $P/P_0 = 0.99$, respectively. X-ray diffraction (XRD) patterns were recorded on a Rigaku Ultima (Japan) using Cu Kα radiation at 40 kV. The 2θ range was between 5° and 90°, with a step of 5°/s. Transmission electron microscope (TEM) images were recorded on a Tecnai G2 (FEI, America) microscope operating at 200 kV, equipped with energy dispersive x-ray energy spectroscopy (EDX). The morphology of catalysts was observed by scanning electron microscope (SEM) on Regulus 8230 (HITACHI, Japan). X-ray photoelectron spectroscopy (XPS) analysis was performed with a K-Alpha spectrometer (Thermo Scientific, America), using Al Kα radiation as an excitation source, and all binding energies were referenced to C 1 s of 284.8 eV. H_2 temperature programmed reduction (H_2-TPR) and H_2 temperature programmed desorption (H_2-TPD) were recorded on AutoChem II 2920 chemical adsorption instrument (Micromeritics, America) to analyze the properties of the active sites.

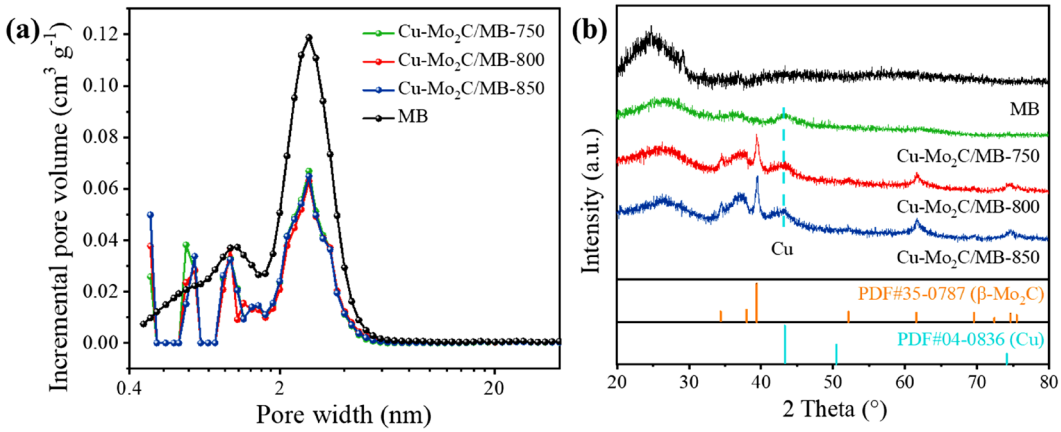

Fig. 1 **a** NLDFT pore size distribution and **b** XRD patterns of MB and 0.8wt.%Cu-20wt.%Mo_2C/MB catalysts

Before analysis, 50 mg catalyst was placed in a U-shaped quartz tube and purged with He for 60 min at 300 °C. Then, the catalyst was cooled to 50 °C. After reaching a stable baseline, the temperature rose from 50 °C to 800 °C at a rate of 10 °C min^{-1} in 10% H_2/Ar atmosphere.

2.4 Catalytic performance

The catalyst performance was evaluated in a fixed-bed reactor. 40 mg granule catalyst (40–80 mesh) was loaded into a stainless-steel reaction tube with an inner diameter of 8 mm. After in-situ reduction in hydrogen atmosphere, the temperature of catalyst bed was adjusted to 400–500 °C, and the specific flow rate for of H_2 and CO_2 gases was controlled according to the set gas hourly space velocity (GHSV) (CO_2:H_2 = 1:2). The gas products were heated at the outlet of the reactor and then entered SHIMADZU GC-2014C gas chromatograph for online analysis, with nitrogen as internal standard. The area normalization method was used for quantitative detection. The calculation formulas of CO_2 conversion rate, CO selectivity, and the reaction rate are shown in Eqs. (1), (2), and (3), respectively.

$$X_{CO_2}(\%) = \frac{n_{CO_2,in} - n_{CO_2,out}}{n_{CO_2,in}} \quad (1)$$

$$S_{CO}(\%) = \frac{n_{CO,out}}{n_{CO,out} + n_{CH_4,out}} \quad (2)$$

$$Rate_{CO_2} = \frac{F_{CO_2} \times X_{CO_2}}{m_{cat}} \quad (3)$$

where:

$n_{CO,out}$ is the flow rate of CO in the outlet reformate;
$n_{CO_2,out}$ is the flow rate of CO_2 in the outlet reformate;
$n_{CH_4,out}$ is the flow rate of CH_4 in the outlet reformate;
$n_{CO_2,in}$ is the flow rate of CO_2 in the feed;
F_{CO_2} is the mole flow rate of CO_2;
m_{cat} is the mass of the catalyst.

3 Results and discussion

3.1 Characterization of catalysts

The N_2 adsorption–desorption isotherms of pristine MB and Cu-Mo_2C/MB catalysts are shown in Fig. S1a, and all samples showed an obvious H4 loop curve in the relative pressure range of 0.4–0.9, indicating that both MB and catalysts present developed mesoporous structures. The NLDFT pore size distributions of MB and catalysts further depicted narrow mesopore diameter distribution of 2–5 nm (Fig. 1a). As can be seen from Table S1, the BET surface area, total pore volume, and mesopore volume of coconut shells-derived ordered MB reached 2693 m^2g^{-1}, 1.56 cm^3g^{-1}, and 0.81 cm^3g^{-1}, respectively. The specific surface area, total pore volume, and mesoporous volume of Cu-Mo_2C/MB catalysts were decreased due to the formation of metal sites on the surface of MB (Wang et al. 2020).

As shown in Fig. 1b, it can be observed that carburizing temperatures influenced the XRD pattern of Cu-Mo_2C/MB catalysts. The broad peaks at around 26.0° and 42.5° can be indexed to the (002) plane of the graphite structure and (100) plane of interlayer condensation, respectively. No Mo_2C peak were observed when the carburizing temperature was 750 °C. As the carburizing temperature reached to 800 °C, the peaks at 2θ of 34.4°, 38.0°, 39.4°, 52.1°, 61.5°, 69.6°, 74.6°, and 75.5° were contributed to the (100), (002), (101), (102), (110), (103), (112), and (201) planes of β-Mo_2C (JCPDS 35–0787), respectively (Nagakura et al. 1966). In addition to the patterns of Mo_2C, the peaks at 43.3° and 50.4° are assigned to Cu sites generated in all samples. The XRD patterns of the Cu-Mo_2C/MB-800 and Cu-Mo_2C/MB-850 catalysts

confirm the effective formation of Cu-Mo_2C sites owing to the carbon framework and reducibility of MB.

With the Cu loading varying from 0.6 to 1.6 wt.% with 20 wt.% Mo_2C, Cu and Mo_2C peaks were clearly observed for Cu-Mo_2C/MB-800 catalysts with high content as shown in Fig. S1b. In addition, Fig. S1c shows the results of different amounts of Cu and Mo_2C in a fixed proportion. It is clear that when the bimetallic content rose, the typical peak strength rose. However, as the loading reached 1.6 wt.% Cu and 40 wt.% Mo_2C, the molybdenum oxide diffraction peak appeared. It could be challenging to entirely carburize molybdenum oxide to generate Mo_2C in the case of high molybdenum concentration.

The Raman patterns and SEM images in Fig. S2 reveal that Cu-Mo_2C/MB catalysts exhibited similar ordering of the carbon and surface morphology at different carburizing temperatures. According to XRD analysis, Mo_2C and Cu active sites could be formed on the surface of MB only when the reduction carburizing temperatures reached 800 and 850 ℃. Therefore, in order to accurately study the morphology, distribution, and mean size of the desired active sites on the surface of MB, Cu-Mo_2C/MB-800 and Cu-Mo_2C/MB-850 were selected in the study for TEM and EDS, and the mapping of these materials are shown in Fig. 2.

With the increase of carburizing reduction temperature, it can be observed from Fig. 2a and b that the average diameter of metal nanoparticles on the surface of the catalyst distinctly increased from 6 to 13 nm, which is consistent with the enhanced diffraction intensity in XRD analysis. The EDS spectra exhibited that the surface Cu, Mo, and O elements of Cu-Mo_2C/MB-800 catalyst were evenly dispersed as shown in Fig. 2d. The species of bimetal nanoparticles on the Cu-Mo_2C/MB-800 catalyst surface were further analyzed by HRTEM, and Fig. 2e and f show that the nanoparticles primarily displayed crystal plane spacing of 0.201 nm and 0.230 nm, which are attributed to Cu (111) crystal plane and Mo (101) crystal plane of β-Mo_2C, respectively (Xiong et al. 2018). These results reveal that highly dispersed nano Cu-Mo_2C interfaces were presented on the surface of Cu-Mo_2C/MB-800.

XPS analyses provided some additional information, such as the element composition and chemical state of various compounds. As shown in Fig. 3a, the Mo 3d XPS spectra for the Cu-Mo_2C/MB catalysts contained three doublets. Doublets with Mo $3d_{5/2}$ peaks at 232.3 ± 0.2 eV were characteristic of Mo^{6+} suggesting the presence of MoO_3 (Cheekatamarla et al. 2005; Choi et al. 1996; Geng et al. 2017; Schaidle et al. 2010; Wei et al. 1998). The peaks at 229.2 ± 0.2 eV are ascribed to Mo^{4+} in MoO_2, while the peaks at 228.5 ± 0.1 eV are assigned to Mo^{2+} in Mo_2C (Ledoux et al. 1992; Mamede et al. 2002). The fitting compositions of Mo and Cu phases were calculated and are summarized in Table S2. The Mo_2C species of catalyst was distinctly enhanced as its carburizing temperature increased from 750 to 800 °C, and enhanced slightly when the temperature was increased from 800 to 850 °C, which was consistent with XRD patterns.

Cu 2p spectra of Cu-Mo_2C/MB catalysts are shown in Fig. 3c. Among these, a peak splitting of 933.8 eV was detected, indicating the possible presence of Cu^0 or/and Cu^+ (Zhang et al. 2019). In order to distinguish the Cu^0 and Cu^+ species, the AES results of catalysts are displayed in Fig. 3d. Two diffraction peaks of 570.2 and 572.8 eV are ascribed to the emission peaks of Cu^0 and Cu^+ respectively, indicating that Cu species in the form of Cu^0 and Cu^+ simultaneously exist on the surface of the catalyst (Tian et al. 2014, 2015). As summarized in Table S2, the Cu^+ contents of Cu-Mo_2C/MB catalysts increased with the enhancement of Mo^{2+} species. This phenomenon further confirms that the strong interaction between Cu and Mo_2C leads to the Cu^+ species generation from Cu^0 via electron transfer, which is in good line with TEM observations. The regulated electronic structure of the Cu species enables the catalyst to exhibit excellent ability to dissociate CO_2 and H_2 molecules, which is conducive to the hydrogenation of CO_2 (Figueras et al. 2021; Zhang et al. 2017).

The redox properties of catalysts are important for CO_2 hydrogenation. Figure 4a displays the results of H_2-TPR investigation into the reducibility of the catalysts. During the reductive process, the H_2 consumption peak of H_2-TPR is related to the reducibility of the corresponding species. The reduction of MoO_3 into MoO_2 and further reduction into Mo_2C caused peaks centered at about 400–500 °C (Liang et al. 2003; Liu et al. 2017). It can be concluded that molybdenum oxide was effectively transformed into Mo_2C with the increase in catalysts carburizing temperature, which is consistent with XRD and XPS investigations. It can be seen from the H_2-TPR results that the catalytic activity of Cu-Mo_2C can be tested effectively by in-situ reduction of the catalyst with H_2 at 500 ℃ after exposure to air (Xiong et al. 2018). In addition, the higher the H_2-TPR peak temperature, the more difficult to reduce the reducible species. The peaks around 740 ℃ may be attributed to the decomposition of non-graphitic carbon, suggesting the high stability of MB during the RWGS reaction.

Besides adsorbing and activating CO_2 molecules, an excellent CO_2 hydrogenation catalyst should have an ideal trade-off between the binding and release of H_2 molecules. As shown in Fig. 4b, the H_2-TPD curves of the catalysts exhibited that two main H_2 desorption peaks (α and β) were formed in the temperature range of 50–550 ℃. The peak at 50 °C indicates the desorption of active

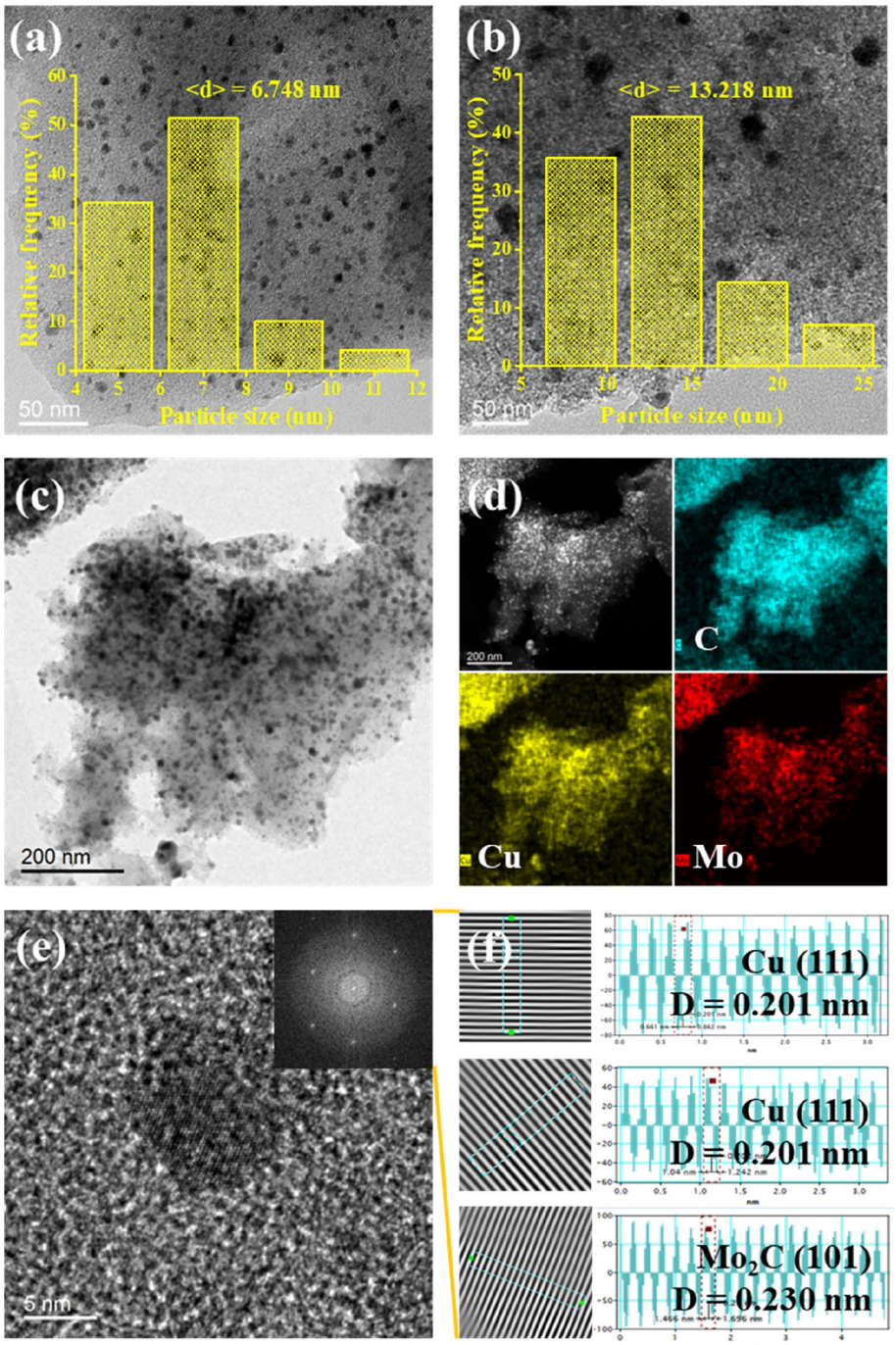

Fig. 2 (**a**–**b**) TEM images of 0.8wt.%Cu-20wt.%Mo_2C/MB-800 and 0.8wt.%Cu-20wt.%Mo_2C/MB-850 at 50 nm (The insets are distributions and mean diameters (< d >) of nanoparticles), (**c**) TEM image of 0.8wt.%Cu-20wt.%Mo_2C/MB-800 catalysts at 200 nm, (**d**) EDS spectra of 0.8wt.%Cu-20wt.%Mo_2C/MB catalyst, (**e**) HRTEM image of 0.8wt.%Cu-20wt.%Mo_2C/MB-800, (**f**) the analysis of lattice fringes

H species by chemisorption on catalyst surfaces owing to the metallic Cu sites (Xu et al. 2021). The big broad peak with a temperature range of 350 to 550 °C suggests the H_2 desorption on the Cu-Mo_2C interface due to the chemically dissociated H species. The additional H_2 desorption peak (γ) for Cu-Mo_2C/MB-750 catalyst may be due to the presence of molybdenum oxide species. When the carburizing temperature increased to 800 and 850 °C, there was only the corresponding H_2 desorption peak of Cu-Mo_2C, indicating that the high carburizing

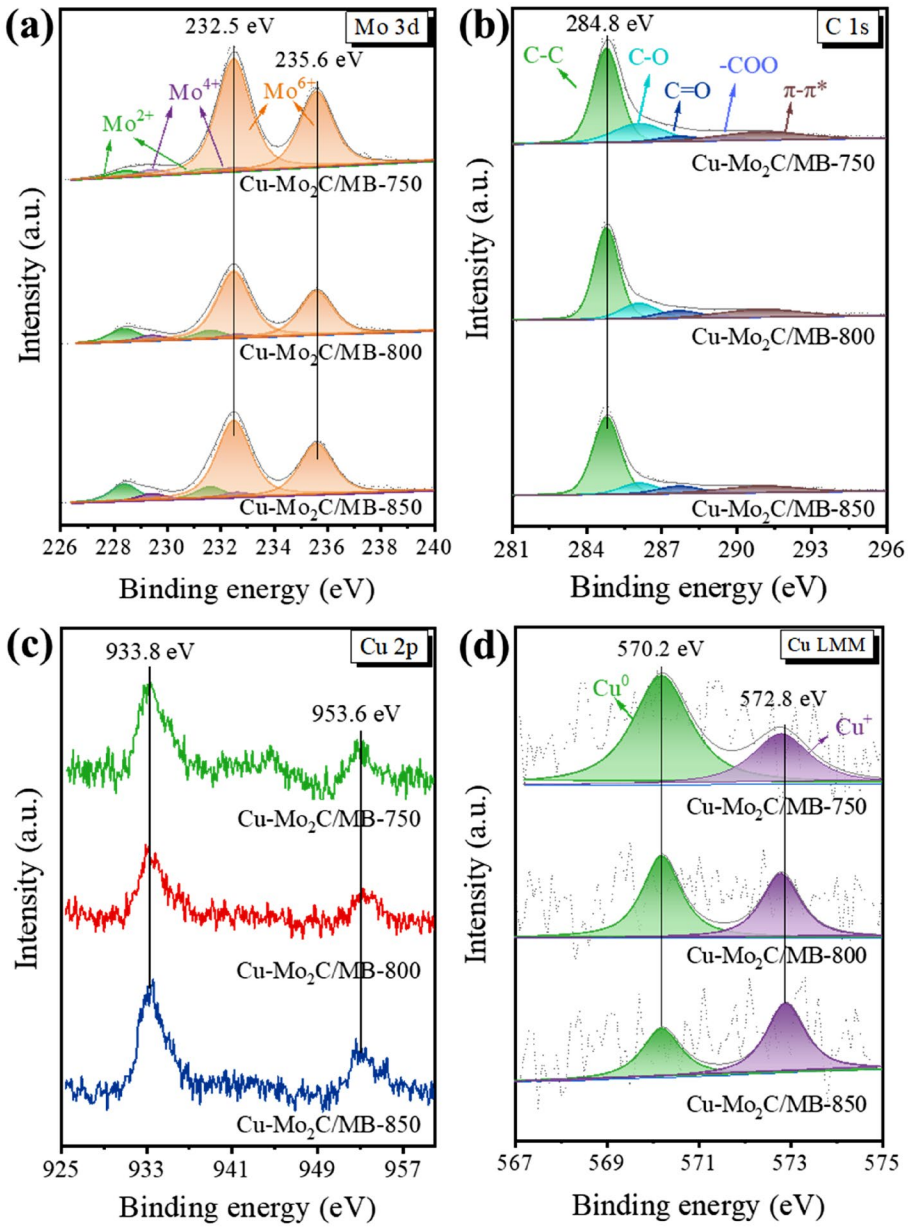

Fig. 3 The XPS spectra of (**a**) Mo 3d, (**b**) C 1 s, (**c**) Cu 2p, and (**d**) Cu AES spectra of 0.8wt.%Cu-20wt.%Mo_2C/MB catalysts

reduction temperature can convert molybdenum oxide to Mo_2C, which is consistent with the results of XRD and XPS. The lower temperature of the H_2 desorption peak for Cu-Mo_2C than Cu-MoO_x reveals that the Cu-Mo_2C species present high activity for chemically dissociating H_2 (Zhang et al. 2022). However, as the carburizing temperature increased from 800 to 850 ℃, the β desorption peak slightly increased to a higher temperature. Considering the TEM results, this might be due to the decrease of Cu-Mo_2C dispersion for Cu-Mo_2C/MB-850. In addition, since the temperature of the H_2 desorption peak for the Cu-Mo_2C interface is lower than the RWGS reaction temperature, it is reasonable to speculate that H_2 could be activated on the surface of Cu-Mo_2C/MB catalysts (Ding et al. 2016).

3.2 Catalytic performance

3.2.1 Evaluation of the catalytic activity

The catalytic performance in RWGS over 0.8wt.%Cu-20wt.%Mo_2C/MB catalysts with different carburizing temperatures was evaluated under the space velocity of 60,000 ml/g/h, V_{CO2}:V_{H2} = 1:2, and the results of CO_2

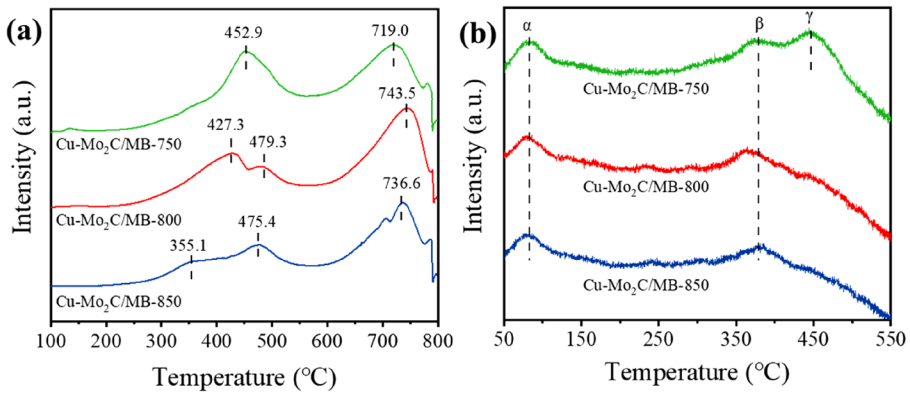

Fig. 4 **a** H_2-TPR and **b** H_2-TPD of 0.8wt.%Cu-20wt.%Mo_2C/MB catalysts

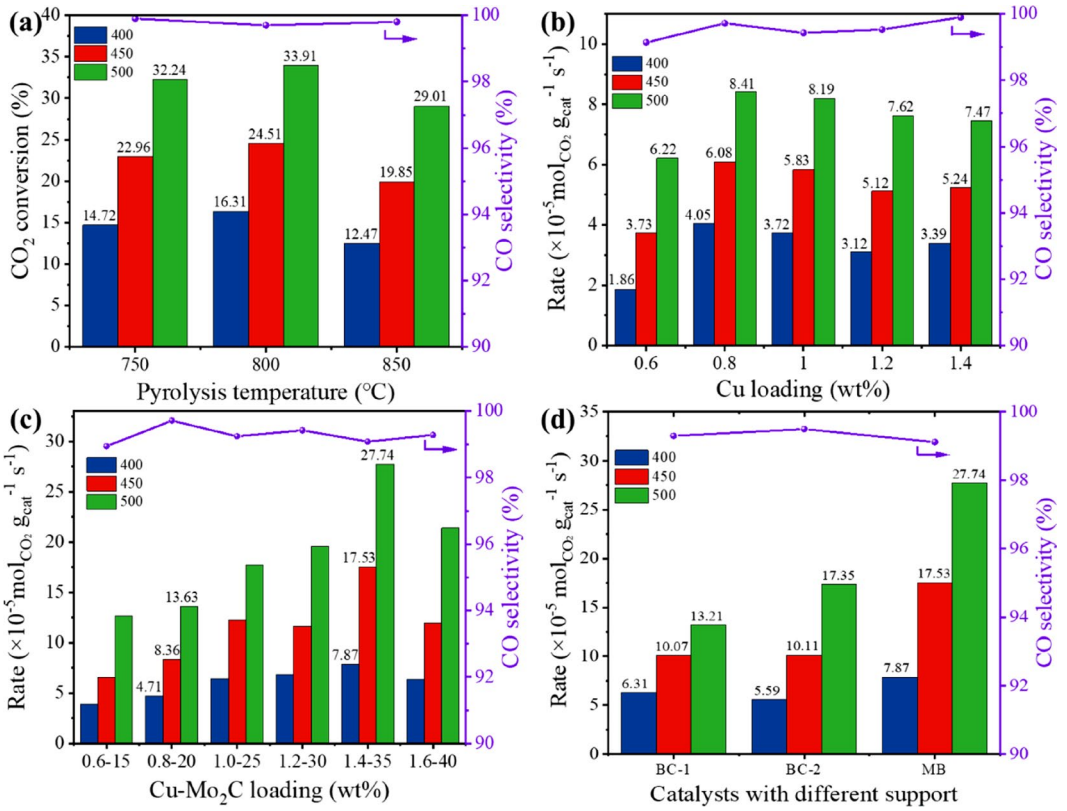

Fig. 5 CO_2 conversion and CO selectivity of RWGS reaction over (**a**) Cu-Mo_2C/MB, (**b** and **c**) Cu-Mo_2C/MB-800 catalysts, and (**d**) other carbon supported Cu-Mo_2C catalysts* at 400, 450, and 500 ℃. Reaction conditions: 0.1 MPa, CO_2:H_2 = 1:2, (**a**, **b**) GHSV = 60,000 ml/g/h, (**c**, d) GHSV = 300,000 ml/g/h. * Catalysts with 1.4 wt.% Cu and 35 wt.% Mo_2C prepared under 800 ℃ carburizing temperature

conversion rate as well as CO selectivity are shown in Fig. 5a. It is noteworthy that the CO selectivity over these prepared Cu-Mo_2C/MB catalysts in this study were all higher than 99.5%. The CO_2 conversion increased with the increase of reaction temperature over Cu-Mo_2C/MB catalysts. This is consistent with the thermodynamic characteristics of RWGS reaction. Meanwhile, the conversion of CO_2 over Cu-Mo_2C/MB catalyst increased with enhancing the carburizing temperature from 750 to 800 °C. Combined with the above characterization results, the interaction between Mo_2C and Cu is stronger than that between MoO_x and Cu, which improves the electron transfer from Cu to Mo (Mo_2C-Cu^+/Cu^0) and generates more electron-deficient states of the Cu species

(Cu^+). This nano Cu-Mo_2C interface exhibited higher adsorption and dissociation of CO_2 and H_2, leading to a promoted RWGS activity over Cu-Mo_2C/MB-800. However, the catalytic activity significantly decreased as carburizing temperature further increased from 800 to 850 °C. This might be due to the distinct agglomeration of Cu-Mo_2C sites on the surface of Cu-Mo_2C/MB-850, resulting in the decrease of accessibility to active sites, reaction molecule adsorption and dissociation, and catalytic activity. It is concluded that moderate carbothermic hydrogen reduction at 800 °C plays a very important role in the formation and high dispersion of Cu-Mo_2C nano-interface on the surface of MB, which further improves its catalytic CO_2 hydrogenation performance.

The Mo_2C content in Cu-Mo_2C/MB-800 catalyst was fixed at 20 wt.% and different Cu loadings were prepared to catalyze the RWGS reaction. The variation of CO_2 conversion and CO selectivity under the reaction conditions of CO_2:H_2 = 1:2 and 60,000 ml/g/h volumetric air velocity are shown in Fig. 5b. At 400–500 °C reaction temperature, the CO_2 conversion rate increased with increasing reaction temperature and its variation was as follows: 0.8wt.%Cu-Mo_2C/MB-800 > 1.0wt.%Cu-Mo_2C/MB-800 > 1.2wt.%Cu-Mo_2C/MB-800 > 1.4wt.%Cu-Mo_2C/MB-800 > 0.6wt.%Cu-Mo_2C/MB-800. The hydrogenation products of each catalyst were concentrated in CO, and the CO selectivity showed a slight change as Cu loading increases. The catalytic performance of catalysts is correlated with their active sites. The activation of the CO_2 and H_2 reactants is effectively facilitated by the Cu transition metal, which serves as the primary active center of the CO_2 catalytic reduction reaction. It is indicated from XRD analysis that the metallic Cu on the catalyst surface still maintained a high dispersion with increasing the Cu loading from 0.6 to 0.8 wt.%. Thus, the improved Cu sites and interaction between Mo_2C and Cu of 0.8wt.%Cu-Mo_2C/MB-800 catalyst promoted the reachability of reactive molecules to the catalytic site and resulted in a high CO_2 conversion rate. It is expected that the accessibility of reactive molecules and active sites as well as their efficiency are improved as the Cu metal loading increases. However, possibly due to the agglomeration of active sites and decreased accessibility of Cu to reactant molecules (Fig. S1b), the catalytic CO_2 conversion rate was reduced as Cu content rose over 1.0 wt.%. Therefore, the 0.8wt.%Cu-Mo_2C/MB-800 catalyst with suitable Cu loading and high dispersion exhibited the best catalytic activity.

It should be noted that the CO_2 conversion achieved over the 0.8wt.%Cu-Mo_2C/MB-800 catalyst at the condition of GHSV = 60,000 ml/g/h was extremely close to the reaction equilibrium at 500 °C (Fig. 0.5a). Thus, the impact of increased Cu-Mo_2C bimetal content on the RWGS reaction was confirmed at GHSV of 300,000 ml/g/h, with an ideal Cu-Mo ratio of 0.8wt.%-20wt.%. This GHSV is a very high condition relative to the operation of the industry (Zhang et al. 2017). Figure 5c demonstrates the link between the activity of the RWGS reaction and the change in bimetal content as follows: 1.4wt.%Cu-35wt.%Mo_2C/MB-800 > 1.6wt.%Cu-40wt.%Mo_2C/MB-800 > 1.2wt.%Cu-30wt.%Mo_2C/MB-800 > 1.0wt.%Cu-25wt.%Mo_2C/MB-800 > 0.8wt.%Cu-20wt.%Mo_2C/MB-800 > 0.6wt.%Cu-15wt.% Mo_2C/MB-800. The experimental findings showed that the CO_2 conversion rate was further improved after an increase in bimetal content, reaching its optimal level at 1.4wt.%-35wt.%. The ultra-high specific surface area and developed mesopore structure of MB can be beneficial to the high metal loading. In addition, through XPS analysis, it was found that the formation of suitable Cu-Mo_2C interaction could be confirmed by the generation of Cu^+. This interaction is responsible for ensuring the high dispersion of surrounding Cu sites while simultaneously elevating Cu-Mo_2C loading, which contributes to the improvement of catalytic performance. Nevertheless, it was discovered that the catalytic activity diminished as the load was increased further. This might be ascribed to the excessive metal load distinctly blocking the pore surface of MB and the formation of molybdenum oxide species revealed from XRD results (Fig. S1c), which reduced catalytic accessibility and activity for the bimetallic interface. In sum up, the 1.4wt.%Cu-35wt.%Mo_2C/MB-800 catalyst exhibited the expectable catalytic activity, with a CO_2 conversion rate of 27.74×10^{-5} $mol_{CO_2}/g_{cat}/s$ and 99.1% CO selectivity at 500 °C.

In order to further investigate the promotion of the porous structure of carbon materials for their catalytic RWGS performances, the catalysts were prepared from BC-1, BC-2, and MB under optimized bimetal loading, and their catalytic results are shown in Fig. 5d. It can be seen that CO_2 conversion rate over Cu-Mo_2C/MB was more than twice that over Cu-Mo_2C/BC-1. The specific surface area, total pore volume, and mesopore volume of BC-1, BC-2, and MB are shown in Fig. 6a and b, and they were distinctly enhanced with consecutive activation. The pore structure of BC-1 after the first stream activation step was mainly micropores and very few mesopores owing to chemical etching of biochar to generate micropores via reaction between H_2O and carbon in the biochar matrix. During the second and third activation processes, the existing micropores of biochar were expanded to create relevant mesopores, and new micropores developed at the same time. Moreover, the content and composition of oxygen-containing functional groups on the surface of BC-1, BC-2, and MB were

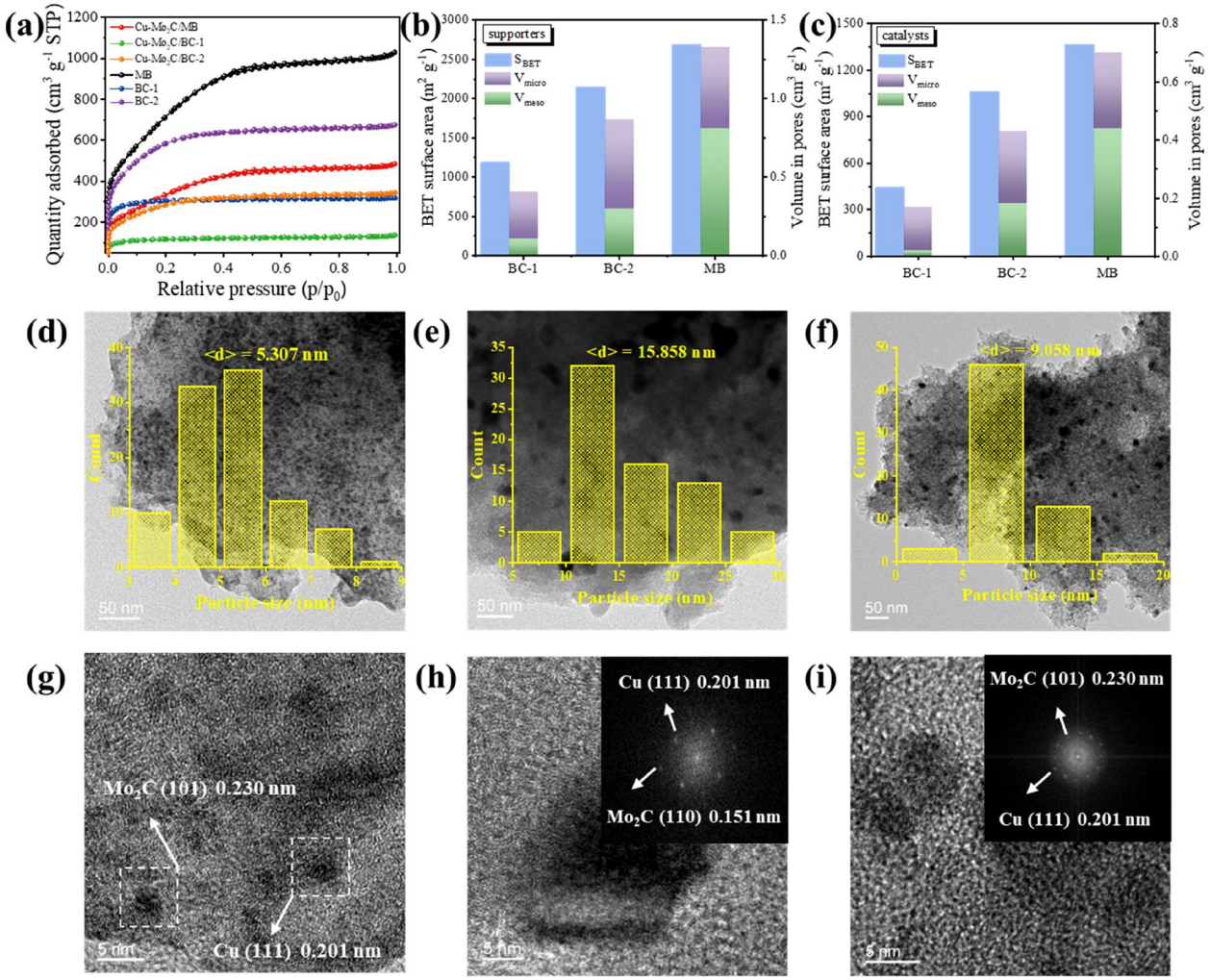

Fig. 6 (**a**) N_2 adsorption–desorption isotherms, (**b**–**c**) the specific surface area, total pore volume, and mesopore volume of BC-1, BC-2, MB, and corresponding catalysts, TEM images (The insets are distributions and mean diameters (< d >) of nanoparticles) at 50 nm of (**d**) Cu-Mo_2C/BC-1, (**e**) Cu-Mo_2C/BC-2, and (**f**) Cu-Mo_2C/MB, HRTEM images at 5 nm of (**g**) Cu-Mo_2C/BC-1, (**h**) Cu-Mo_2C/BC-2, and (**i**) Cu-Mo_2C/MB

similar according to the O 1 s and C 1 s XPS results (Fig. S3). After the loading of 1.4 wt.% Cu and 35 wt.% Mo_2C, the Cu-Mo_2C/MB catalyst still exhibited much higher specific surface area and mesopore volume than Cu-Mo_2C/BC-1 and Cu-Mo_2C/BC-2 catalysts (Fig. 6c). As depicted in Fig. 6d-i, the mean particle size of Cu-Mo_2C bimetal sites on the surface of BC-1, BC-2, and MB were 5.307, 15.808, and 9.058 nm, respectively. This result suggests that high microporosity benefits the metal dispersion due to the confinement effect (Luo et al. 2020), as well as ultra-high specific surface area and pore volume. However, owing to the much lower specific surface area and pore volume of Cu-Mo_2C/BC-1, the CO_2 conversion rate over Cu-Mo_2C/BC-1 was lower than that over Cu-Mo_2C/MB-800. According to the results of Fig. 5d and Fig. 6, it is obvious that the ultrahigh specific surface area and mesopore volume of MB greatly facilitate the dispersal of high bimetal loading, CO_2 adsorption, unobstructed pore for mass transfer and accessibility of active sites to reaction molecules, resulting in the excellent CO_2 conversion rate of RWGS reaction over 1.4wt.%Cu-35wt.%Mo_2C/MB-800 catalyst (Wen et al. 2024).

As listed in Table S3, the catalyst created in this work had a much higher CO_2 conversion rate at very low H_2 partial pressure than recently reported Cu-Mo_2C and other metal-based catalysts. This may be owing to the prepared coconut shell derived MB support, whose high surface area and mesopore volume are beneficial for the dispersion of nano Cu-Mo_2C interface, CO_2 adsorption, and diffusion rate of reactant molecule. Under the

condition of low CO_2/H_2 ratio and ultrahigh GHSV, the catalytic conversion of CO_2 into CO at atmospheric can be achieved with high efficiency and selectivity.

3.2.2 Stability of the catalyst

Only a catalyst with high reactivity and stability can be applied in industry. The 1.4wt.%Cu-35wt.%Mo_2C/MB-800 catalyst was tested for 50 h under the conditions of V_{CO_2}:V_{H_2} = 1:2, GHSV = 300,000 ml/g/h and 500 ℃ reaction temperature. The Fig. S4a demonstrates that the CO_2 conversion rate stayed constant at about 27.7×10^{-5} $mol_{CO_2}/g_{cat}/s$ without decrease of activity. This suggests that the interaction between Mo_2C and Cu on the MB surface prevents the leaching and agglomeration of the active site. Meanwhile, the CO selectivity remained stable over 99.1%. In order to delve into the structural evolution of used Cu-Mo_2C/MB-800 catalyst, the XRD, TEM, Raman, and XPS (Mo 3d, C 1 s, Cu 2p and Cu AES) characterizations for the spend catalyst after 50 h reaction were further carried out ((Fig. S4b-c, Fig. S5, and Fig. S6)). The XRD diffraction peaks of used catalyst exhibited similar Cu and Mo_2C crystalline phases as observed on the fresh catalyst (Fig. S4b). The maintained I_D/I_G according to the Raman patterns suggested the fixation of carbon ordering of biochar support (Fig. S4c). The comparison of Mo, C, and Cu species in the used and fresh Cu-Mo_2C/MB-800 catalyst also showed the stability of biochar support and Cu-Mo_2C bimetal sites, which was determined by XPS results (Fig. S5a-d). Meanwhile, as shown in TEM images and elemental mapping images (Fig. S6a-c), the used Cu-Mo_2C/MB-800 catalyst showed the homogeneous distribution of Cu and Mo throughout the entire MB surface, and constant nano Cu-Mo_2C interfaces of about 9 nm mean diameter compared with the fresh catalyst (Fig. 6f). These results indicate Cu-Mo_2C interfaces and MB support were in good stability. In conclusion, the 1.4wt.%Cu-35wt.%Mo_2C/MB-800 catalyst exhibited remarkable catalytic activity, selectivity, and stability.

4 Conclusion

A coconut shell derived ordered MB with ultrahigh surface area and mesopore volume (2–5 nm) was designed and utilized as the carbon source of carburization reduction and support for Cu-Mo_2C bimetal sites. This MB promoted the construction of dispersed nano Cu-Mo_2C interface and molecule diffusion on the surface of the catalyst. The carburization reduction of MoO_x to dispersed Mo_2C strengthened the interaction between Cu and Mo_2C, which improved the electron transfer from Cu to Mo (Cu^+/Cu^0-Mo_2C) and increased electron-deficient states of the Cu species (Cu^+). This fabricated Cu-Mo_2C nano-interface exhibited superb adsorption and selective activation of reaction molecules and high anchoring of Cu sites. Overall, coupling nano Cu-Mo_2C interface with MB favored the exceptional activity, selectivity, and stability of RWGS over Cu-Mo_2C/MB-800 catalyst at very low H_2 partial pressure.

Supplementary Information

The online version contains supplementary material available at https://doi.org/10.1007/s42773-024-00392-5.

Supplementary file 1.

Acknowledgements

We would like to thank the funding of National Natural Science Foundation of China and National Key Research and Development Program of China. We would like to express our gratitude to all those who helped us during the writing of this paper.

Author contributions

Xueyuan Pan: Methodology, Investigation, Writing – original draft, Data curation. Hao Sun: Conceptualization, Writing – review & editing, Funding acquisition. Mingzhe Ma: Investigation, Data curation. Haiquan Liao: Investigation, Writing – original draft. Guowu Zhan: Writing – review & editing. Kui Wang: Writing – review & editing. Mengmeng Fan: Writing – review & editing. Jingcheng Xu: Investigation. Linfei Ding: Investigation, Data curation. Kang Sun: Supervision. Jianchun Jiang: Supervision, Project administration. The authors read and approved the final manuscript.

Funding

This study was funded by National Natural Science Foundation of China (32101474, 42377249) and National Key Research and Development Program of China (2023YFD2201605).

Availability of data and materials

Data will be made available on request.

Declarations

Competing interests

The authors declare that they have no known competing financial interests or personal relationships that could have appeared to influence the work reported in this paper.

Author details

[1]Key Lab. of Biomass Energy and Material, Jiangsu Province, Key and Open Lab. of Forest Chemical Engineering, SFA, National Engineering Lab. for Biomass Chemical Utilization, Institute of Chemical Industry of Forest Products, Chinese Academy of Forestry, Nanjing 210042, China. [2]Academy of Advanced Carbon Conversion Technology, College of Chemical Engineering, Huaqiao University, Xiamen 361021, Fujian, China. [3]Co-Innovation Center of Efficient Processing and Utilization of Forest Resources, Nanjing Forestry University, Nanjing 210042, China.

Received: 14 April 2024 Revised: 24 September 2024 Accepted: 28 September 2024
Published online: 23 October 2024

References

Ahmadi Khoshooei M, Wang X, Vitale G, Formalik F, Kirlikovali KO, Snurr RQ, Pereira-Almao P, Farha OK (2024) An active, stable cubic molybdenum carbide catalyst for the high-temperature reverse water-gas shift reaction. Science 384:540–546. https://doi.org/10.1126/science.adl1260

Borghei M, Laocharoen N, Kibena-Põldsepp E, Johansson L-S, Campbell J, Kauppinen E, Tammeveski K, Rojas OJ (2017) Porous N, P-doped carbon

from coconut shells with high electrocatalytic activity for oxygen reduction: Alternative to Pt-C for alkaline fuel cells. Appl Catal B Environ 204:394–402. https://doi.org/10.1016/j.apcatb.2016.11.029
Cheekatamarla PK, Thomson WJ (2005) Poisoning effect of thiophene on the catalytic activity of molybdenum carbide during tri-methyl pentane reforming for hydrogen generation. Appl Catal A 287:176–182. https://doi.org/10.1016/j.apcata.2005.03.043
Chen K, Li Y, Wang M, Wang Y, Cheng K, Zhang Q, Kang J, Wang Y (2021) Functionalized carbon materials in syngas conversion. Small 17:e2007527. https://doi.org/10.1002/smll.202007527
Choi JG, Thompson LT (1996) XPS study of as-prepared and reduced molybdenum oxides. Appl Surf Sci 93:143–149. https://doi.org/10.1016/0169-4332(95)00317-7
Ding R, Wu Y, Chen Y, Chen H, Wang J, Shi Y, Yang M (2016) Catalytic hydrodeoxygenation of palmitic acid over a bifunctional Co-doped MoO_2/CNTs catalyst: an insight into the promoting effect of cobalt. Catal Sci Technol 6:2065–2076. https://doi.org/10.1039/c5cy01575h
Figueras M, Gutierrez RA, Vines F, Ramirez PJ, Rodriguez JA, Illas F (2021) Supported molybdenum carbide nanoparticles as an excellent catalyst for CO_2 hydrogenation. ACS Catal 11:9679–9687. https://doi.org/10.1021/acscatal.1c01738
Gawande MB, Fornasiero P, Zboril R (2020) Carbon-based single-atom catalysts for advanced applications. ACS Catal 10:2231–2259. https://doi.org/10.1021/acscatal.9b04217
Geng W, Han H, Liu F, Liu X, Xiao L, Wei W (2017) N, P, S-codoped C@nano-Mo2C as an efficient catalyst for high selective synthesis of methanol from CO2 hydrogenation. J CO2 Util. https://doi.org/10.1016/j.jcou.2017.06.016
Juneau M, Vonglis M, Hartvigsen J, Frost L, Bayerl D, Dixit M, Mpourmpakis G, Morse JR, Baldwin JW, Willauer HD, Porosoff MD (2020) Assessing the viability of K-Mo_2C for reverse water-gas shift scale-up: molecular to laboratory to pilot scale. Energy Environ Sci 13:2524–2539. https://doi.org/10.1039/d0ee01457e
Kunkes EL, Studt F, Abild-Pedersen F, Schloegl R, Behrens M (2015) Hydrogenation of CO_2 to methanol and CO on Cu/ZnO/Al_2O_3: Is there a common intermediate or not? J Catal 328:43–48. https://doi.org/10.1016/j.jcat.2014.12.016
Ledoux MJ, Cuong PH, Guille J, Dunlop H (1992) Compared activity of platinum and high specific surface-area Mo2C and WC catalysts fpr reforming reactions.1. catalyst activation and stabilization-reaction of normal-hexane. J Catal 134:383–398. https://doi.org/10.1016/0021-9517(92)90329-g
Len T, Luque R (2023) Addressing the CO_2 challenge through thermocatalytic hydrogenation to carbon monoxide, methanol and methane. Green Chem 25:490–521. https://doi.org/10.1039/d2gc02900f
Li Z, Wu W, Wang M, Wang Y, Ma X, Luo L, Chen Y, Fan K, Pan Y, Li H, Zeng J (2022) Ambient-pressure hydrogenation of CO_2 into long-chain olefins. Nat Commun 13:2396. https://doi.org/10.1038/s41467-022-29971-5
Liang CH, Ma WP, Feng ZC, Li C (2003) Activated carbon supported bimetallic CoMo carbides synthesized by carbothermal hydrogen reduction. Carbon 41:1833–1839. https://doi.org/10.1016/s0008-6223(03)00169-6
Liu X, Song Y, Geng W, Li H, Xiao L, Wu W (2016) Cu-Mo_2C/MCM-41: an efficient catalyst for the selective synthesis of methanol from CO_2. Catalysts 6:75. https://doi.org/10.3390/catal6050075
Liu X, Kunkel C, Ramirez de la Piscina P, Homs N, Vines F, Illas F (2017) Effective and highly selective CO generation from CO_2 using a polycrystalline alpha-Mo_2C catalyst. ACS Catal 7:4323–4335. https://doi.org/10.1021/acscatal.7b00735
Liu Y, Deng D, Bao X (2020) Catalysis for selected C1 chemistry. Chem 6:2497–2514. https://doi.org/10.1016/j.chempr.2020.08.026
Liu HX, Li SQ, Wang WW, Yu WZ, Zhang WJ, Ma C, Jia CJ (2022) Partially sintered copperceria as excellent catalyst for the high-temperature reverse water gas shift reaction. Nat Commun 13:867. https://doi.org/10.1038/s41467-022-28476-5
Luo E, Wang C, Li Y, Wang X, Gong L, Zhao T, Jin Z, Ge J, Liu C, Xing W (2020) Accelerated oxygen reduction on Fe/N/C catalysts derived from precisely-designed ZIF precursors. Nano Res 13:2420–2426. https://doi.org/10.1007/s12274-020-2868-8
Mamede AS, Giraudon JM, Lofberg A, Leclercq L, Leclercq G (2002) Hydrogenation of toluene over beta-Mo_2C in the presence of thiophene. Appl Catal A 227:73–82. https://doi.org/10.1016/s0926-860x(01)00923-1
McLaughlin H, Littlefield AA, Menefee M, Kinzer A, Hull T, Sovacool BK, Bazilian MD, Kim J, Griffiths S (2023) Carbon capture utilization and storage in review: Sociotechnical implications for a carbon reliant world. Renew Sustain Energy Rev 177:113215. https://doi.org/10.1016/j.rser.2023.113215
Mejia CH, van Deelen TW, de Jong KP (2018) Activity enhancement of cobalt catalysts by tuning metal-support interactions. Nat Commun 9:4459. https://doi.org/10.1038/s41467-018-06903-w
Nagakura S, Kikuchi M, Oketani S (1966) Electron diffraction determination of ionization of carbon atom in beta-Mo_2C crystal. Acta Crystallogr 21:1009–1010. https://doi.org/10.1107/s0365110x66004407
Posada-Perez S, Ramirez PJ, Gutierrez RA, Stacchiola DJ, Vines F, Liu P, Illas F, Rodriguez JA (2016) The conversion of CO_2 to methanol on orthorhombic beta-Mo_2C and Cu/beta-Mo_2C catalysts: mechanism for admetal induced change in the selectivity and activity. Catal Sci Technol 6:6766–6777. https://doi.org/10.1039/c5cy02143j
Reddy KP, Dama S, Mhamane NB, Ghosalya MK, Raja T, Satyanarayana CV, Gopinath CS (2019) Molybdenum carbide catalyst for the reduction of CO_2 to CO: surface science aspects by NAPPES and catalysis studies. Dalton Trans 48:12199–12209. https://doi.org/10.1039/c9dt01774g
Schaidle JA, Lausche AC, Thompson LT (2010) Effects of sulfur on Mo_2C and Pt/Mo_2C catalysts: Water gas shift reaction. J Catal 272:235–245. https://doi.org/10.1016/j.jcat.2010.04.004
Song L, Wang H, Wang S, Qu Z (2023) Dual-site activation of H_2 over Cu/$ZnAl_2O_4$ boosting CO_2 hydrogenation to methanol. Appl Catal B Environ 322:122137. https://doi.org/10.1016/j.apcatb.2022.122137
Sun H, Sun K, Wang F, Liu Y, Ding L, Xu W, Sun Y, Jiang J (2021) Catalytic self-activation of Ca-doped coconut shell for in-situ synthesis of hierarchical porous carbon supported CaO transesterification catalyst. Fuel 285:119192. https://doi.org/10.1016/j.fuel.2020.119192
Sun H, Ma MZ, Fan MM, Sun K, Xu W, Wang K, Li BJ, Jiang JC (2022) Controllable preparation of biomass derived mesoporous activated carbon supported nano-CaO catalysts for biodiesel production. Energy 261:125369. https://doi.org/10.1016/j.energy.2022.125369
Tawalbeh M, Javed RMN, Al-Othman A, Almomani F (2023) The novel contribution of non-noble metal catalysts for intensified carbon dioxide hydrogenation: Recent challenges and opportunities. Energy Conv Manag 279:116755. https://doi.org/10.1016/j.enconman.2023.116755
Tian X, Wang T, Yang Y, Li Y-W, Wang J, Jiao H (2014) Structures and energies of Cu clusters on Fe and Fe_3C surfaces from density functional theory computation. PhysChemChemPhys 16:26997–27011. https://doi.org/10.1039/c4cp04012k
Tian X, Wang T, Yang Y, Li Y-W, Jiao H (2015) Surface morphology of Cu adsorption on different terminations of the hagg iron carbide (chi-Fe_5C_2) phase. J Phys Chem C 119:7371–7385. https://doi.org/10.1021/acs.jpcc.5b01324
Wang F, Jiang J, Wang K, Zhai Q, Long F, Liu P, Feng J, Xia H, Ye J, Li J, Xu J (2019) Hydrotreatment of lipid model for diesel-like alkane using nitrogen-doped mesoporous carbon-supported molybdenum carbide. Appl Catal B Environ 242:150–160. https://doi.org/10.1016/j.apcatb.2018.09.077
Wang F, Zhang W, Jiang J, Xu J, Zhai Q, Wei L, Long F, Liu C, Liu P, Tan W, He D (2020) Nitrogen-rich carbon-supported ultrafine MoC nanoparticles for the hydrotreatment of oleic acid into diesel-like hydrocarbons. Chem Eng J 382:122464. https://doi.org/10.1016/j.cej.2019.122464
Wang H, Bootharaju MS, Kim JH, Wang Y, Wang K, Zhao M, Zhang R, Xu J, Hyeon T, Wang X, Song S, Zhang H (2023a) Synergistic interactions of neighboring platinum and iron atoms enhance reverse water-gas shift reaction performance. J Am Chem Soc 145:2264–2270. https://doi.org/10.1021/jacs.2c10435
Wang Y, Sun J, Tsubaki N (2023b) Clever nanomaterials fabrication techniques encounter sustainable C1 catalysis. Acc Chem Res 56:2341–2353. https://doi.org/10.1021/acs.accounts.3c00311
Wei ZBZ, Grange P, Delmon B (1998) XPS and XRD studies of fresh and sulfided Mo_2N. Appl Surf Sci 135:107–114. https://doi.org/10.1016/s0169-4332(98)00267-0
Wen M, Sun N, Jiao L, Zang S-Q, Jiang H-L (2024) Microwave-assisted rapid synthesis of MOF-based single-atom Ni catalyst for CO_2 electroreduction at ampere-level current. Angew Chem Int Ed 63:e202318338. https://doi.org/10.1002/anie.202318338
Wu W, Wang Y, Luo L, Wang M, Li Z, Chen Y, Wang Z, Chai J, Cen Z, Shi Y, Zhao J, Zeng J, Li H (2022) CO_2 hydrogenation over Copper/ZnO single-atom

catalysts: Water-promoted transient synthesis of methanol. Angew Chem Int Ed 61:e202213024. https://doi.org/10.1002/anie.202213024

Xiong K, Zhou G, Zhang H, Shen Y, Zhang X, Zhang Y, Li J (2018) Bridging Mo_2C–C and highly dispersed copper by incorporating N-functional groups to greatly enhance the catalytic activity and durability for carbon dioxide hydrogenation. J Mater Chem A 6:15510–15516. https://doi.org/10.1039/c8ta04096f

Xu J, Gong X, Hu R, Liu Z-w, Liu Z-t (2021) Highly active K-promoted Cu/β-Mo_2C catalysts for reverse water gas shift reaction: effect of potassium. Mol Catal 516:111954. https://doi.org/10.1016/j.mcat.2021.111954

Zhang X, Zhu X, Lin L, Yao S, Zhang M, Liu X, Wang X, Li Y-W, Shi C, Ma D (2017) Highly dispersed copper over beta-Mo_2C as an efficient and stable catalyst for the reverse water gas shift (RWGS) reaction. ACS Catal 7:912–918. https://doi.org/10.1021/acscatal.6b02991

Zhang Q, Pastor-Perez L, Jin W, Gu S, Reina TR (2019) Understanding the promoter effect of Cu and Cs over highly effective beta-Mo_2C catalysts for the reverse water-gas shift reaction. Appl Catal B Environ 244:889–898. https://doi.org/10.1016/j.apcatb.2018.12.023

Zhang X, Zhang M, Deng Y, Xu M, Artiglia L, Wen W, Gao R, Chen B, Yao S, Zhang X, Peng M, Yan J, Li A, Jiang Z, Gao X, Cao S, Yang C, Kropf AJ, Shi J, Xie J, Bi M, van Bokhoven JA, Li YW, Wen X, Flytzani-Stephanopoulos M, Shi C, Zhou W, Ma D (2021) A stable low-temperature H_2-production catalyst by crowding Pt on alpha-MoC. Nature 589:396–401. https://doi.org/10.1038/s41586-020-03130-6

Zhang Y, He Y, Cao M, Liu B, Li J (2022) High selective methanol synthesis from CO_2 hydrogenation over Mo-Co-C-N catalyst. Fuel 325:124854. https://doi.org/10.1016/j.fuel.2022.124854